Oxysulfate, oxysulfide, and oxide red-phosphors from one single hydroxyl sulfate precursor $(Gd,Eu)_2(OH)_4SO_4 \cdot nH_2O$: phase evolution, and photoluminescence

Bowen Wang,[a] Changshuai Gong,[a] Jiantong Wang,[a] Xuejiao Wang,[a*] Ji-Guang Li[b*]

[a]College of Chemistry and Materials Engineering, Bohai University, Jinzhou, Liaoning 121007, China

[b]Research Center for Electronic and Optical Materials, National Institute for Materials Science, Tsukuba, Ibaraki 305-0044, Japan

*Corresponding author

Dr. Xuejiao Wang
Bohai University
Jianzhou, China
Tel: +86-416-3400708
E-mail: wangxuejiao@bhu.edu.cn

Dr. Ji-Guang Li
National Institute for Materials Science
Ibaraki, Japan
Tel: +81-29-860-4394
E-mail: li.jiguang@nims.go.jp

Abstract

Three kinds of important red phosphors, the monoclinic $Ln_2O_2SO_4$ (Ln=Gd, Eu), cubic Ln_2O_3 and hexagonal Ln_2O_2S were obtained through controlled calcination of single hydroxyl sulfate $Ln_2(OH)_4SO_4 \cdot nH_2O$ (LLnHs) precursor. The conditions of the hydrothermal synthesis of LGdHs were investigated, and it was found that LGdHs can be obtained in pH range of 7-9. The micro-morphology changes from aggregated spheres to micro plates with increasing pH. $Gd_2(OH)_4SO_4 \cdot nH_2O$ was transformed into $Gd_2O_2SO_4$ *via* removal of hydration water (up to 340 ^oC) and dehydroxylation (340-800 ^oC), and finally change into Gd_2O_3 *via* desulfuration (800-1230 ^oC) in the air. Gd_2O_2S was obtained from $Gd_2(OH)_4SO_4 \cdot nH_2O$ by calcination in reducing atmosphere (800-1200 ^oC). Photoluminescence excitation (PLE) studies showed broad and strong O-Eu CT bands at 260, 275, and 267 nm in Ln_2O_3, $Ln_2O_2SO_4$ and Ln_2O_2S, respectively, and extra S-Eu CT band locates at 334 nm was observed in Ln_2O_2S. The strongest red emission corresponding to the electric dipole $^5D_0 \rightarrow {}^7F_2$ transitions of the Eu^{3+} ions were observed at 613, 618, and 626 nm in Ln_2O_3, $Ln_2O_2SO_4$ and Ln_2O_2S system, respectively. The quenching concentration of Ln_2O_2S (3%) is smaller than those of $Ln_2O_2SO_4$ (6%) and Ln_2O_3 (6%), which is due to the fact that the average Eu^{3+}-Eu^{3+} distance is smaller in Ln_2O_2S. The quenching mechanism was investigated, and it was found that the observed luminescence quenching was dominated by exchange interactions among Eu^{3+} ions.

Keywords: Photoluminescence, oxysulfate, oxysulfide, hydroxyl sulfate

1. Introduction

Due to the unique physicochemical properties of rare-earth elements, phosphors activated by rare earth are being actively studied for a wide range of applications, including high-performance optical display, luminescence, optoelectronic devices, sensors, and magnets [1-8]. The synthesis route significantly influences the properties of rare earth doped materials, such as morphology, fluorescence intensity, and quantum efficiency. Various methodologies were developed, including solid-state reaction, molten salt method, combustion synthesis method, hydrothermal and so on [9-12]. Amongst, solid-state reaction is the most efficient method for design and synthesis of phosphors, but elevated temperature is always needed. Another widely applied route is hydrothermal method, through which final products were always obtained *via* calcination of certain intermediate precursors. It has the merits of controlled morphology and low processing temperature, however, in most cases only one product was obtainable *via* such route. We found in this work that $Ln_2(OH)_4SO_4{\cdot}nH_2O$ can serve as an efficient precursor, and through its controlled calcination three kinds of important phosphors, including oxysulfide Ln_2O_2S, oxysulfate $Ln_2O_2SO_4$ and oxide Ln_2O_3 can be obtained. Rare earth doped Ln_2O_2S is an important kind of phosphors, founding application in many fields, such as lighting, MRI, scintillant and biological labeling [13,14]. Meanwhile, $Ln_2O_2SO_4$ with a layered structure was reported as a promising material for large volume oxygen storage [15-17] as well as a useful luminescent material [18-20]. The $Ln_2(OH)_4SO_4{\cdot}nH_2O$ crystals have the same Ln:S molar ratio of the above-mentioned two types of phosphors, and thus, they may be directly converted into the target phosphors under proper conditions, without any additional use of hazardous sulfurization reagents. Furthermore, after the decomposition of sulfate ions

by calcining LLnHs at higher temperatures in the air, Ln_2O_3 luminescence materials can be obtained.

In this work, $(Gd,Eu)_2(OH)_4SO_4 \cdot nH_2O$ compounds with tunable morphology were hydrothermally obtained, and through the controlled calcination, three kinds of important red phosphors $(Gd,Eu)_2O_2SO_4$, $(Gd,Eu)_2O_3$ and $(Gd,Eu)_2O_2S$ were obtained. The influence of pH level on the phase and micro-morphology of hydrothermal products, and photoluminescent properties of the resultant phosphors were system studied based on the analyses of X-ray diffractometry (XRD), field emission scanning electron microscopy (FE-SEM), Fourier transform infrared spectroscopy (FTIR), thermogravimetry/differential scanning calorimetry (TG/DSC) and photoluminescence (PL/PLE) results.

2. Experimental Procedure

2.1 Reagents and sample synthesis

The reagents for the synthesis are Ln_2O_3 (Ln = Eu, Gd, 99.99% pure), $(NH_4)_2SO_4$, $NH_3 \cdot H_2O$, and HNO_3. The rare earth oxide were bought from Huizhou Ruier Rare Chemical Hi-Tech Co. Ltd. (Huizhou, China), and the other reagents were from Shenyang Chemical Reagent Factory (Shenyang, China). All the chemicals were used as received without further purification. Stock solutions of $Ln(NO_3)_3$ (Ln=Gd and Eu) were prepared by dissolving Gd_2O_3 and Eu_2O_3 in concentrated HNO_3 (0.1 M). In a typical synthetic procedure, 6 mmol $(NH_4)_2SO_4$ was dissolved in 60 ml mixed nitrate solution (6 mmol) under magnetic stirring for 10 min. $NH_3 \cdot H_2O$ was then dropwise added into the mixed solution to reach the designed pH. The resultant mixture was continuously stirred for 10 min before being transferred to a Teflon lined stainless steel autoclave of 100 ml capacity. The autoclave was put in an electric oven preheated to

120 °C for a reaction period of 24 h. After the reaction, the hydrothermal product was collected *via* centrifugation. The wet precipitate was thoroughly washed with water and ethanol, and it was finally dried in air at 50 °C for 12 h. The $(Gd_{1-x}Eu_x)_2(OH)_4SO_4{\cdot}nH_2O$ compound was calcined in the air and hydrogen atmosphere at 1200 °C to obtain final $(Gd_{1-x}Eu_x)_2O_3$ and $(Gd_{1-x}Eu_x)_2O_2S$ red phosphors (heating rate 10 °C /min), respectively. The $(Gd_{1-x}Eu_x)_2O_2SO_4$ sulfate was obtained by calcining the LLnH in the air at 1000 °C with the same heating rate.

2.2 Characterization

Phase identification was performed *via* powder XRD (Model PW3040/60, Philips, Eindhoven, The Netherlands) using nickel filtered CuK_α radiation operated at 40 kV/40 mA. Morphologies were observed *via* field emission scanning electron microscopy by an JSM-7001F (JEOL, Tokyo, Japan) operated at 10 kV. Phase decomposition of the LLnH was made in flowing simulated air (heating rate: 10 °C/min) *via* TG/DSC (Model STI409PC, NETZSCH, Germany) analysis. FTIR analyses (Model 4200, JASCO, Tokyo) were performed by the standard KBr method. Photoluminescence spectra and fluorescence decay kinetics of phosphors were performed at room temperature using an FP-6500 fluorescence spectrophotometer (JASCO, excitation source: 150 W Xe lamp).

Results and discussion

Fig. 1 shows XRD patterns of products hydrothermally synthesized at 120 °C with different pHs (7.0-10.0). Products synthesized at lower pHs of 7.0-9.0 are indexable to $Gd_2(OH)_4SO_4{\cdot}nH_2O$ (SO_4^{2-}-LLnHs) [21,22] even though the diffraction peak in the same position of the products exhibit some difference in intensity which may be caused by the difference of morphology as analyzed later (Fig. 3). Previously, we investigated the hydrothermal synthesis conditions of $La_2(OH)_4SO_4{\cdot}nH_2O$ which can be

hydrothermally obtained at 120 °C and pH of 9.0 - 10.0 [23]. The Ln^{3+} cations undergo hydration and hydrolysis in an aqueous solution to form six-fold coordinated $[Ln(OH)_x(H_2O)_y(SO_4)_z]_{3-x-z/2}$ ($x+y+z=6$) complex species [24]. Compared with lanthanum, gadolinium has a smaller ion radius (for 9-fold coordination, La^{3+} and Gd^{3+} have respective ionic sizes of 0.1216 and 0.1107 nm) [25] which promotes hydrolysis of Gd^{3+} at same pH thus favoring the formation of $Gd_2(OH)_4SO_4 \cdot nH_2O$ at lower pHs than $La_2(OH)_4SO_4 \cdot nH_2O$.

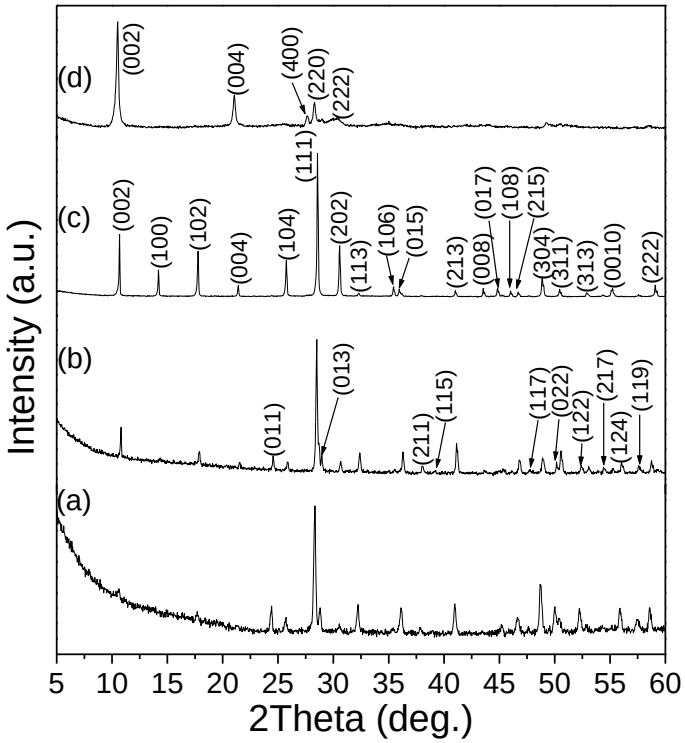

Fig. 1. XRD patterns of the hydrothermal products synthesized at 120 °C under different pHs, with (a) pH=7.0, (b) pH=8.0, (c) pH=9.0, and (d) pH=10.0.

Fig. 1d is the product synthesized at higher pH of 10.0 and it conforms well to the layered compound of $Gd_2(OH)_5X \cdot nH_2O$ (X=Cl^- or NO_3^-) [26-29]. Combined the FTIR behavior (Fig.2d) of this product, it can be concluded that the product obtained here is sulfate type, the $Ln_2(OH)_5(SO_4)_{0.5} \cdot nH_2O$. The compound synthesized at pH of 9.0 shows

better crystallinity and morphology, and thus, in this work Eu^{3+} doped $Gd_2(OH)_4SO_4{\cdot}nH_2O$ were synthesized according to the above mentioned hydrothermal route at 120 °C and pH = 9.0. The Eu^{3+} content in the ($Gd_{1-x}Eu_x$) combination was varied in the range of x=0.03-0.07 to reveal its effects on optical properties (Fig. S1).

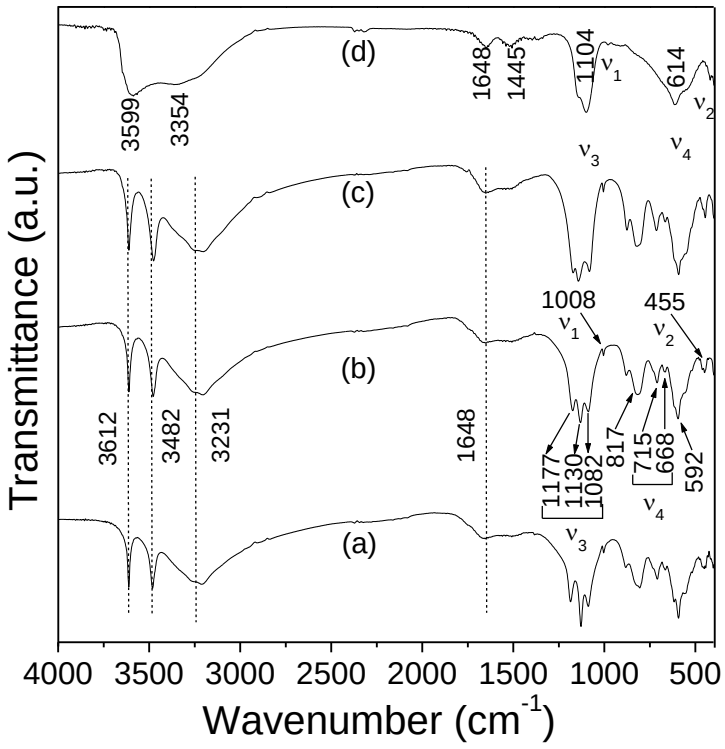

Fig. 2. FTIR spectra of the hydrothermal products synthesized at 120 °C under different pHs, with (a) pH=7.0, (b) pH=8.0, (c) pH=9.0, and (d) pH=10.0.

Fig. 2 compares the FTIR behaviors of the $Gd_2(OH)_4SO_4{\cdot}nH_2O$ (pH = 7-9 products) and $Gd_2(OH)_5SO_4{\cdot}nH_2O$ (pH = 10 product). The $Gd_2(OH)_4SO_4{\cdot}nH_2O$ obtained at different pHs (Figs. 2a-c) shows similar hydroxides, hydrogen water, and sulfate ions vibrations, however, striking different behaviors were observed in $Gd_2(OH)_5(SO_4)_{0.5}{\cdot}nH_2O$ (Fig. 2d). The fundamental vibrations of SO_4^{2-} are located at 1104 (ν_3), 981 (ν_1), 618 (ν_4) and 451 cm^{-1} (ν_2), according to [4]. The SO_4^{2-} vibrations are all clearly observable for the two kinds of LLnHs but with ν_3 and ν_4 vibrated obviously

different. In $Gd_2(OH)_4SO_4 \cdot nH_2O$, ν_3 and ν_4 modes split into separated sharp peaks indicating the distortion and trans-bidentate ligands chelating of tetrahedron sulfate ion [4]. The distortion of the SO_4^{2-} tetrahedron in $Gd_2(OH)_4SO_4 \cdot nH_2O$ was believed to arise from intra-molecular H_2O/SO_4^{2-} interactions *via* hydrogen bonding. While in $Gd_2(OH)_5(SO_4)_{0.5} \cdot nH_2O$, the ν_3 (1104 cm^{-1}) and ν_4 (614 cm^{-1}) vibrations are non-splitting, and it indicates that the sulfate ions in $Gd_2(OH)_5(SO_4)_{0.5} \cdot nH_2O$ are not directly coordinated to rare earth ions. However, ν_1 and ν_2 vibrations are observable and imply that the SO_4^{2-} tetrahedron is not totally free but slightly distorted. The absorptions at ~3354, and 1648 cm^{-1} are attributed to O-H stretching vibration (ν_1 and ν_3) and H-O-H bending vibration mode (ν_2) of hydration water, and vibration at 3599 cm^{-1} is arising from hydroxyl (OH^-) groups (Fig. 2d) [30-32]. While in spectra (a)-(c), except the similar observed vibrations at 3231 and 1648 cm^{-1}, additional hydroxyl absorption appears at 3612, 817 and 592 cm^{-1}. The reason is that the SO_4^{2-} interacts with H_2O *via* hydrogen bonding which would distort not only the SO_4^{2-} but also the molecular structure of H_2O [4,21].

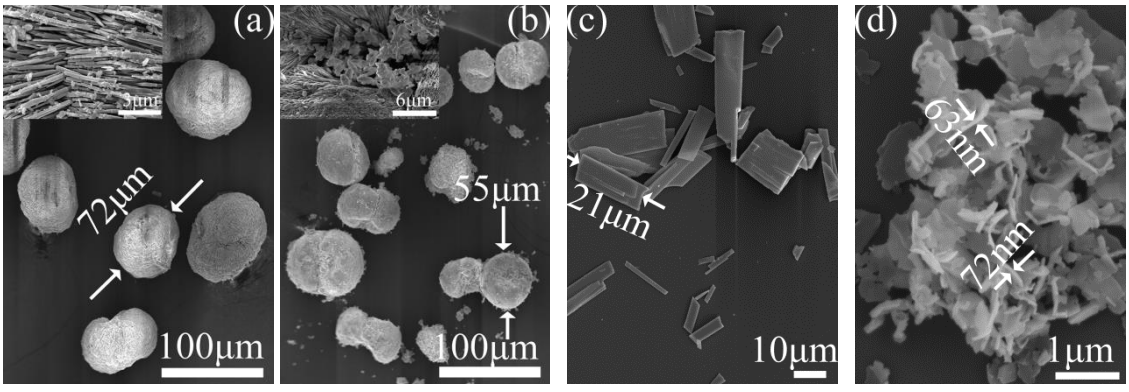

Fig. 3. FE-SEM images of the hydrothermal products synthesized at 120 °C under different pHs, with (a) pH=7.0, (b) pH=8.0, (c) pH=9.0, and (d) pH=10.0.

The pH level significantly influences the morphology of the hydrothermal products, as shown in Fig. 3. Raising the pH level of the reaction system obviously downsizes the

particles of final products. The reason behind the shrunken particle size is the increasing pH raises the nucleation number. The LLnHs obtained at the lowest pH of ~7.0 show the microsphere morphology (~70-90 μm), which, in fact, is the aggregated small plates (insert in Fig. 3a), and with relatively uniform size. When pH is ~8.0, the aggregated spheres were also obtained but with smaller particle size ~40-60 μm and more loose aggregation. The formation of the aggregated spheres can be explained as followed: the tetrahedral sulfate ions are abundant in negative charges and oxygen ions, and consequently, the sulfate ions attract positive groups. The nucleation and growth of small LLnHs plates are adhered to the sulfate ions, and due to the attraction, the final products are appeared as aggregated microspheres. But with the continued increasing pH, the attraction becomes weaker or even disappears, and so, the crystal can grow freely and show the nature of layered compounds which explains the formation of microplates. The LLnHs compounds were reported to construct by alternative stacking of the bidentated sulfate layer and the corrugated two-dimensional layer formed by LnO_9 polyhedra parallel to the (001) plane [22]. When aggregate to the microsphere at pH of 7.0 and 8.0, the edge of the plates is exposured in the surface of the microplates, as shown in the insets. This makes the intensity of the (111) plane much stronger than the (002) plane. When crystallized freely as a microplate, the intensity ratio of the (002)/(111) obviously increases due to the exposure of the plates. In Fig. 1, this explains the peak intensity difference of the same phases obtained at different pHs. $Gd_2(OH)_5(SO_4)_{0.5}\cdot nH_2O$ synthesized at pH of 10.0 (image d) is crystallize as thin nano-platelets.

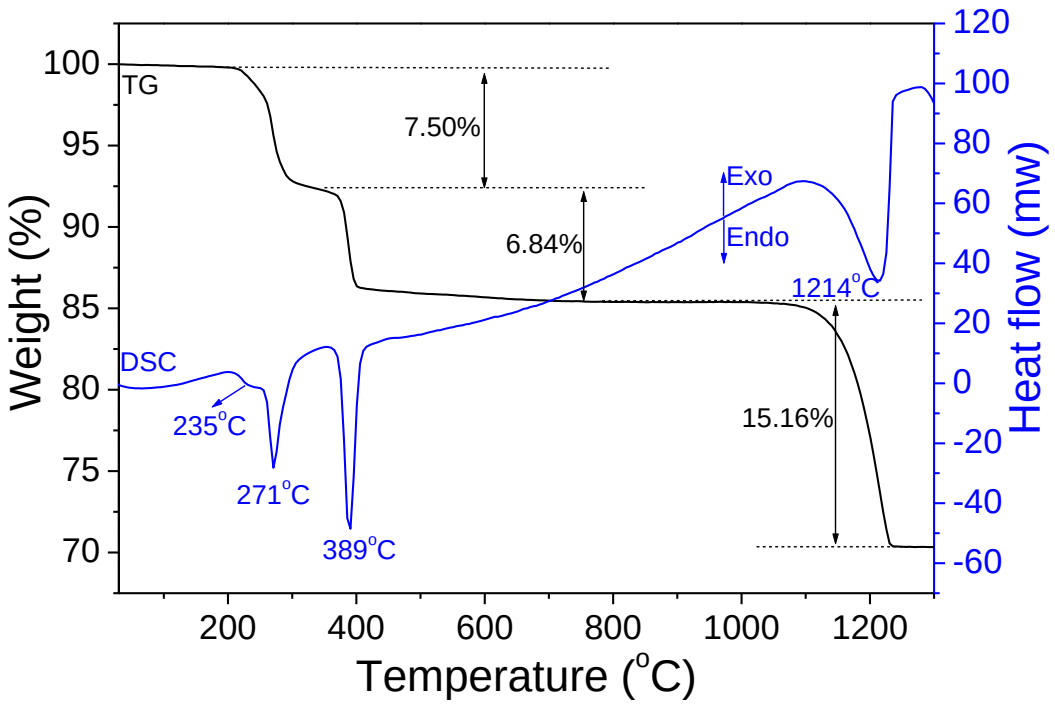

Fig. 4. TG/DSC curves of microplates precursor synthesized at 120 °C and pH of ~9.0.

Fig. 4 shows TG/DSC curves of the microplates $Gd_2(OH)_4SO_4 \cdot nH_2O$ sample obtained in flowing simulated air (5 ml/min, heating rate: 10 °C/min). The compound lost weight in three main separate steps upon heating. The initial removal of hydration water is observed up to 340 °C with a total weight loss of 7.50% and an endothermic peak at 271 °C, from which the hydration number *n* was derived to be ~2.15. The weight loss of 6.84% took place in the range of ~340-800 °C, accompanied by a sharp endotherm at ~389 °C, which can be attributed to dehydroxylation of the hydroxides layers (calculated weight loss: 6.96%). Compared with the thermal behavior of $La_2(OH)_4SO_4 \cdot nH_2O$ reported before [33-35], the dehydroxylation reaction which involved the breaking of Gd^{3+}-OH^- bonding of $Gd_2(OH)_4SO_4 \cdot nH_2O$ proceeded at higher temperatures indicating the higher stability in hydroxides layers for smaller lanthanides. The mass stays stable up to ~1030 °C, followed by further decomposition of $Gd_2O_2SO_4$ to form cubic Gd_2O_3, accompanied by an endotherm at ~1214 °C (calculated weight loss:

15.46%; observed weight loss: 15.16%). The weak endotherm at ~235 °C on the DSC curve is due to the evaporation of surface adsorbed water. According to the above analysis, the LGdHs compound decomposes to cubic Gd_2O_3 according to the following main stages:

$Gd_2(OH)_4SO_4 \cdot 2.15H_2O \rightarrow Gd_2(OH)_4SO_4 + 2.15H_2O$ (up to 340 °C)

$Gd_2(OH)_4SO_4 \rightarrow Gd_2O_2SO_4 + 2H_2O$ (340-800 °C)

$Gd_2O_2SO_4 \rightarrow Gd_2O_3 + SO_3$ (800-1230 °C)

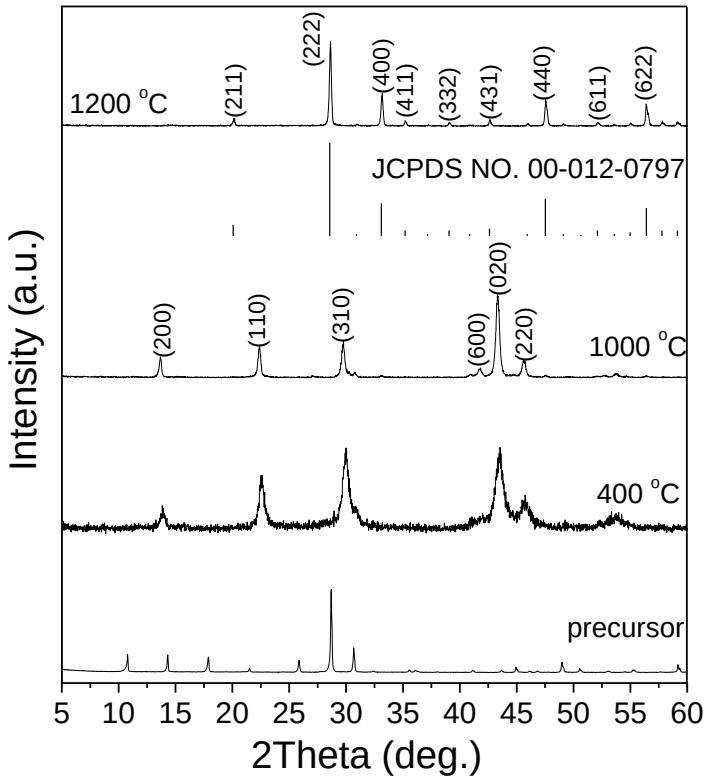

Fig. 5. XRD patterns of the microplate precursor and the products obtained in the air by calcination at different temperatures for 1 h.

Phase evolution of the microplates precursor upon calcination in the air is shown in Fig. 5. The calcination at 400-1000 °C produces monoclinic $Gd_2O_2SO_4$ as a pure phase [16,21]. Narrow peak shapes and improved peak intensities are observed at a 1000 °C owing to high lattice perfection and crystallite growth. The continued calcination at

higher temperature 1200 °C yielded cubic Gd_2O_3 (JCPDS No.00-012-0797) [36]. Thus, in this work, the $(Gd_{1-x}Eu_x)_2O_2SO_4$ and $(Gd_{1-x}Eu_x)_2O_3$ phosphors were obtained by calcining the corresponding $L(Gd_{1-x}Eu_x)Hs$ precursors in the air at 1000 and 1200 °C, respectively (Figs. S2 and S3). The phase transformation of LGdHs to $Gd_2O_2SO_4$ was viewed as the removal of hydrogen water and hydroxyl groups. The LnO_9 polyhedra transformed into LnO_4 tetrahedra linked together by sharing edges. The monoclinic $Gd_2O_2SO_4$, which inherits the layered structure, was built up *via* alternative stacking of the Gd-O-Gd and SO_4^{2-} layers along the a-axis [11]. The morphology evolution of the LGdHs calcined in the air at different temperatures is shown in Fig. S4 (Supporting information). The calcination products can mainly preserve the morphology of layered precursor in the calcination process even at so high temperature as 1200 °C. However, cracks and pores were found in the products calcined at 1000 and 1200 °C.

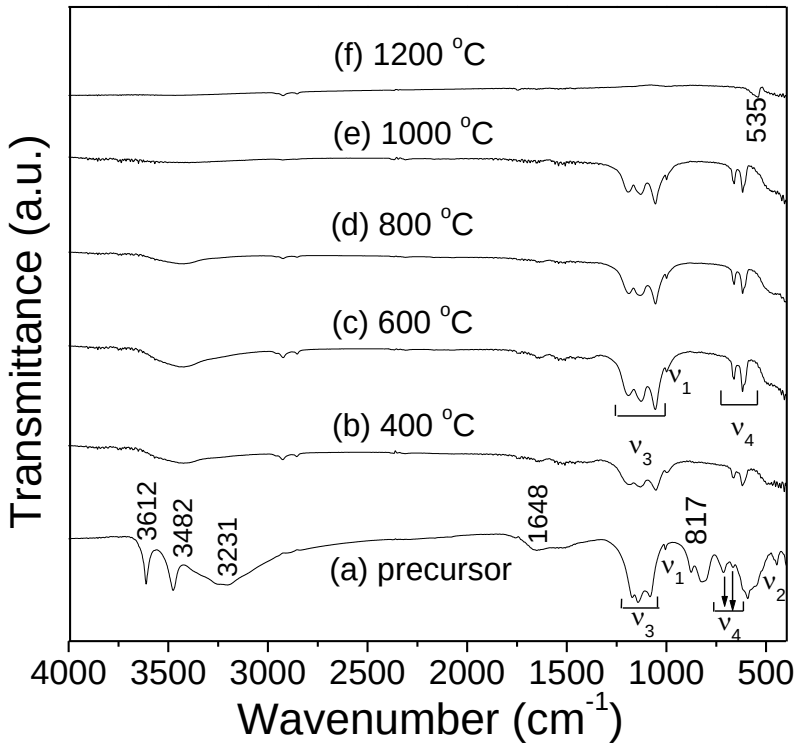

Fig. 6. FTIR spectra of the microplates precursor and its products calcined in the air at different temperatures for 1 h.

To further investigate the change of functional groups, the FTIR results recorded for the precursor and calcination products are shown in Fig. 6. As it can be assumed on the base of spectra shown in Fig. 2 the vibrations of hydroxyl units, water molecule and coordinate sulfate ions are observed in Fig. 6a. Compared with spectrum (a), the absence of hydroxyl vibrations in Figs. 6b-e indicates that the dehydroxylation occurred in this temperature range. However, residual wide bands present at ~3500 cm^{-1} up to 800 °C, this may due to the absorbed water from the ambient atmosphere by the samples. The fundamental ν_3 and ν_4 modes of sulfate ion with splitting were still observable even after calcination at 1000 ^oC indicating the similar configuration of sulfate ions in the oxysulfate and LGdHs. However, expansion of the ν_3 band from ~1165-1078 to ~1205-1054 cm^{-1} and obviously sharper split of ν_4 band are observed in the oxysulfate. These effects are mainly caused by dehydration and dihydroxylation, which remove the intramolecular SO_4^{2-}/OH^- (H_2O) coupling and enhance SO_4^{2-} coordination with rare earth ions. In Fig. 6f, only the Gd-O vibration (~535 cm^{-1}) can be observed, and it further indicates the decomposition of sulfate ions at a 1200 ^oC with formation of the pure oxide. The FTIR behaviors observed here correspond well to the thermal behaviors and the phase evolution of the LGdHs (Figs. 4 and 5).

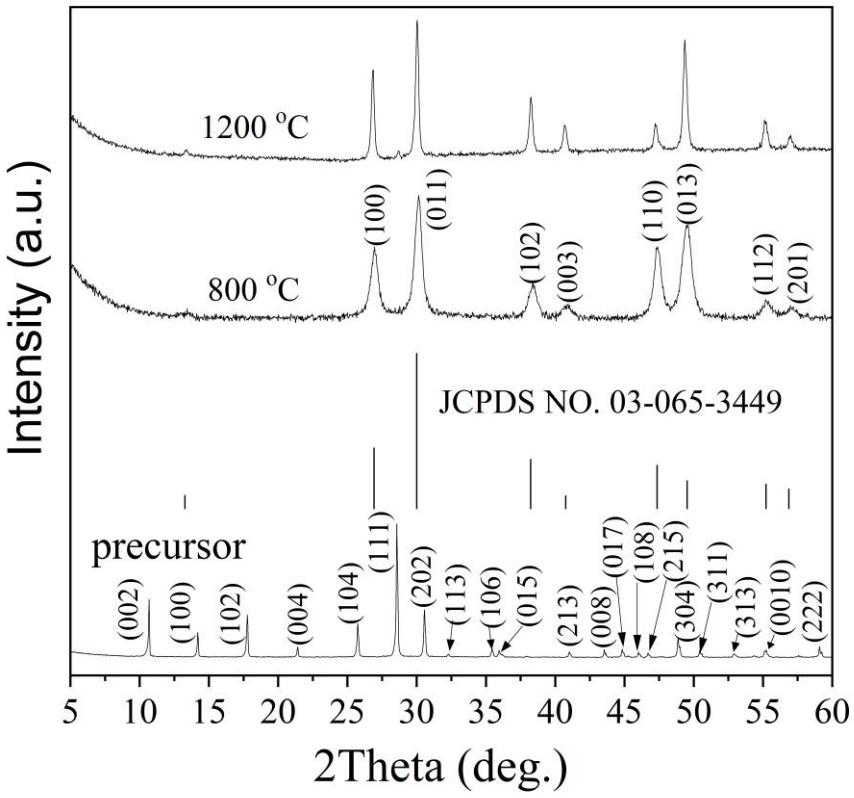

Fig. 7. XRD patterns of the microplates precursor and its products calcined in hydrogen atmosphere at different temperatures for 1 h. The standard diffractions of Gd_2O_2S (JCPDS No. 03-065-3449) are included as bars for comparison.

Fig. 7 exhibits XRD patterns of LGdHs and the products calcined under flowing H_2 at different temperatures for 1 h. The 800-1200 °C powders can all be well indexed to hexagonal structured Gd_2O_2S (JCPDS No. 03-065-3449) [37]. It is reasonable to infer that the LGdHs precursor converted into Gd_2O_2S through the $Gd_2O_2SO_4$ as an intermediate phase, as was reported earlier for L(La,Eu)Hs [23]. The phase transformation of $Gd_2O_2SO_4$ to Gd_2O_2S can be viewed as the removal of oxide ions surrounding sulfur as a result of the reduction, and thus, the two phase share a similar structure: alternative stacking of a $Gd_2O_2^{2+}$ layer and a layer of anion groups, i.e. sulfate (SO_4^{2-}) or sulfide (S^{2-}). As TG/DSC and XRD results showed no phase change of

$Gd_2O_2SO_4$ in the air up to ~1000 °C, the above observations thus indicate that H_2 has a strong capability to take out oxygen atoms from SO_4^{2-} even at the low temperature of 800 °C. Thus, the $(Gd_{1-x}Eu_x)_2O_2S$ phosphors were obtained upon annealing the LLnHs precursors in flowing H_2 at 1200 °C (Fig. S5).

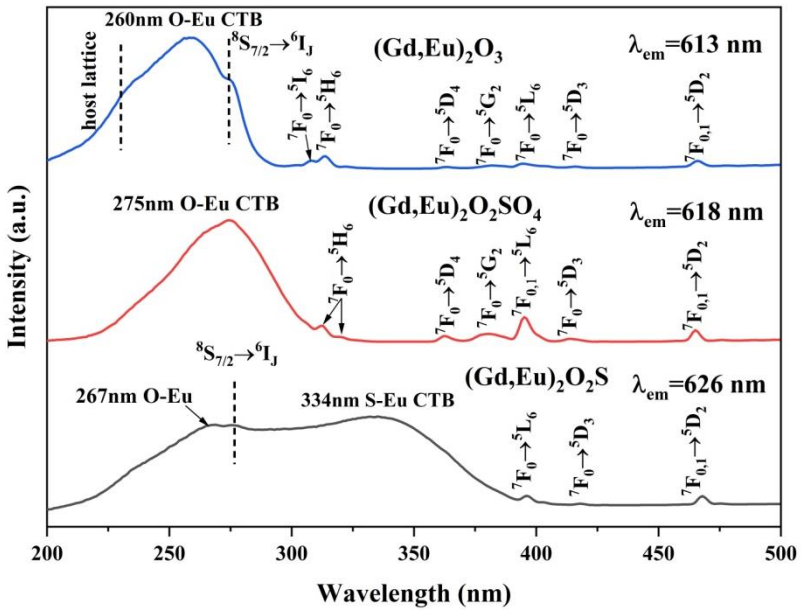

Fig. 8. PL excitation spectra of the $(Gd_{0.97}Eu_{0.03})_2O_2SO_4$, $(Gd_{0.97}Eu_{0.03})_2O_3$ and $(Gd_{0.97}Eu_{0.03})_2O_2S$ red phosphors converted from the microplate precursors.

Fig. 8 shows the photoluminescence excitation spectra of the $(Gd_{0.97}Eu_{0.03})_2O_2SO_4$, $(Gd_{0.97}Eu_{0.03})_2O_3$ and $(Gd_{0.97}Eu_{0.03})_2O_2S$ red phosphors converted from the microplate LLnHs precursor, and the PLE spectra recorded for other compositions are shown in Fig. S6. A glance at the three spectra is yielded that all the spectra consist of two parts i.e. the broad and strong charge transfer (CT) excitations and relatively weaker and sharper *f-f* transitions in the longer wavelengths, as labeled in the spectra [38-42]. In Gd_2O_2S crystal structure, an additional stronger S-Eu CT excitation band, aside from the O-Eu one, is observed as a broad band center around 344 nm, which makes the oxysulfide compounds show significantly broader CT excitation ranges. While the $4f^6$ transitions are located at almost the same position even though in Gd_2O_2S host lattice, some $4f^6$

transitions are indistinguishable due to the overlapping with much stronger CT band. The reason is that $4f^6$ electrons are well shielded from the surroundings by completely filled $5s^2$ and $5p^6$ orbitals [43,44]. The $^8S_{7/2}\rightarrow{}^6I_J$ transition of Gd^{3+} ions is observed at ~276 nm [45] for Gd_2O_2S and Gd_2O_3, and for $Gd_2O_2SO_4$ the $^8S_{7/2}\rightarrow{}^6I_J$ transition overlaps with the CT band.

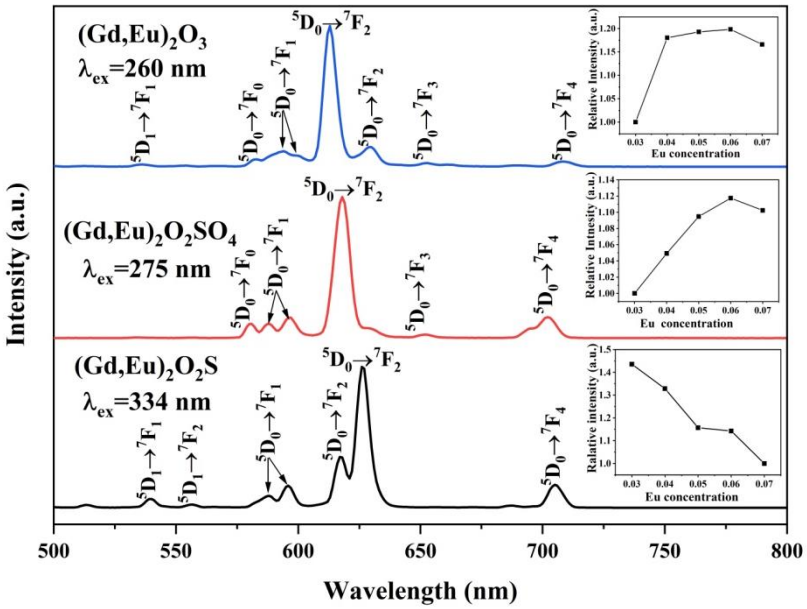

Fig. 9. PL emission spectra of the $(Gd_{0.97}Eu_{0.03})_2O_2SO_4$, $(Gd_{0.97}Eu_{0.03})_2O_3$, and $(Gd_{0.97}Eu_{0.03})_2O_2S$ red phosphors converted from the microplates precursors.

Fig. 9 displays the photoluminescence emission spectra of the $(Gd_{0.97}Eu_{0.03})_2O_2SO_4$, $(Gd_{0.97}Eu_{0.03})_2O_3$ red phosphors excited by the $O^{2-}\rightarrow Eu^{3+}$ CTB, and $(Gd_{0.97}Eu_{0.03})_2O_2S$ phosphor excited by $S^{2-}\rightarrow Eu^{3+}$ CTB. Sharp peaks are observed over the 500-730 nm range, which are associated with the transitions from the excited $^5D_0$ and $^5D_1$ state to the ^7F_J (J =0, 1, 2) emission states of Eu^{3+} [46-48]. The strongest red emission corresponding to the electric dipole $^5D_0\rightarrow{}^7F_2$ transitions of the Eu^{3+} ions were observed at 613, 618, and 626 nm, as reported before [18,49,50] for $(Gd,Eu)_2O_3$, $(Gd,Eu)_2O_2SO_4$, and $(Gd,Eu)_2O_2S$ respectively. The $(Gd_{0.97}Eu_{0.03})_2O_2S$ phosphors emit red light at 626

nm, which is closer to the ideal red-color (around 650 nm) than the other two host lattices at around 615 nm. The emission spectra measured for other phosphor compositions are shown in Fig. S7. For each host lattice, the PL bands do not change obviously in their positions but exhibit different intensities with the varying doping concentration. For $(Gd_{1-x}Eu_x)_2O_2SO_4$ and $(Gd_{1-x}Eu_x)_2O_3$ phosphors, the intensity of the strongest emission increases up to ~6% and then decreases, indicating that the optimal Eu^{3+} content (quenching concentration) is 6 at %. For Gd_2O_2S host, the PL intensity decreases with the increase of the doping concentration from 3 at% and according to the following analysis, we assume that in this system the optimal doping concentration is 3%. Similar optimal doping concentrations for the three systems were reported before [49,51,52]. The optimal doping concentration observed here corresponds well with the value inferred from the Ozawa's empirical formula as analyzed later in Fig.10b.

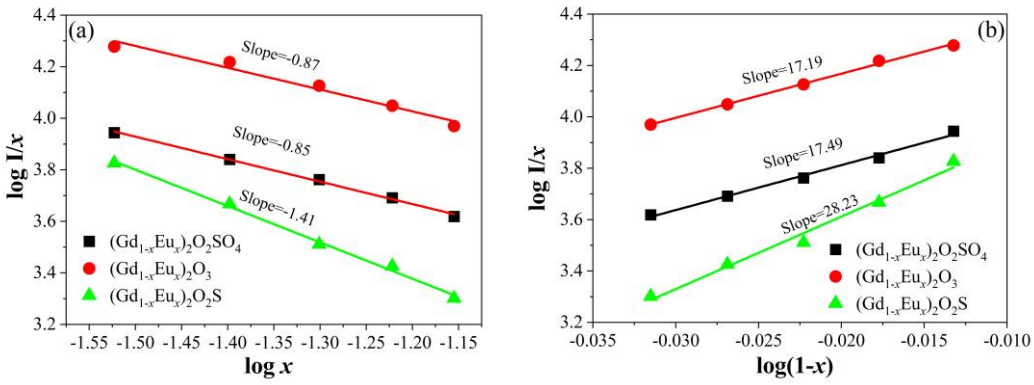

Fig. 10. The relationship between log(I/*x*) and log(*x*) and the relationship between log(I/*x*) and log(1-*x*) for the $(Gd_{1-x}Eu_x)_2O_2SO_4$, $(Gd_{1-x}Eu_x)_2O_3$, and $(Gd_{1-x}Eu_x)_2O_2S$ red phosphors calcined from the SO_4^{2-}-LGdHs precursors.

By analyzing the index of electric multipole (*s*), the mutual interaction type of luminescence quenching can be inferred. The *s* value can be obtained according to the equation log(I/*x*)=(-s/d)log*x*+logf [53,54], where I is the emission intensity, d is the sample dimension, *x* is the activator content and f is a constant independent of activator

content. The *s* values of 3, 6, 8 and 10 is related to the mechanism of exchange interaction, the dipole-dipole, dipole-quadrupole and quadrupole-quadrupole electric interactions, respectively. The log(I/*x*)-log(*x*) plots for the $(Gd,Eu)_2O_2SO_4$, $(Gd,Eu)_2O_3$, and $(Gd,Eu)_2O_2S$ phosphors are given in Fig. 10a. From the plots, slope (-*s*/3) of -0.85, -0.87 and -1.41 are derived, yielding *s* values of around 2.55, 2.61 and 4.23 for the three systems. This indicates that the observed luminescence quenching is dominantly resulted from exchange interactions for the energy transfer among Eu^{3+} ions, possibly *via* a phonon-assisted three activated ions nonresonant interaction' mechanism [54,55].

The luminous intensity of luminescence materials is closely correlated to the activator concentration and depends on the interaction between rare earth ions i.e. the quenching mechanism. According to Ozawa [56], if the luminescence quenching mechanism is governed by exchange interactions of the rare earth ions, the quenching concentration can be estimated according to 1/(1+Z), which can be derived from the following equation: log(I/*x*)=logb+Zlog(1-*x*), where I is the emission intensity, *x* is the Eu^{3+} content, b is an independent constant and Z represented the number of nearest-neighbor cations surrounding the luminescent center ions. The log(I/*x*)-log(1-*x*) plots (Fig. 10b) yield slopes Z=17.49, 17.19, and 28.23 for $(Gd_{1-x}Eu_x)_2O_2SO_4$, $(Gd_{1-x}Eu_x)_2O_3$ and $(Gd_{1-x}Eu_x)_2O_2S$ phosphors, respectively. It can be obtained that 1/(1+Z) values are approximately 0.054, 0.054 and 0.034 which are nearly consistent with the quenching concentration of Eu^{3+} observed in the three systems (Fig. 9). The initial increase of the emission intensity is due to the emergence of more luminescence centers with increasing Eu^{3+} concentration. The further doping of Eu^{3+} shortens the distances among Eu^{3+} ions, and thus, the probability of energy transfer among the Eu^{3+} ions is enhanced which increases the emission intensity. But luminescence quenching occurred with

higher doped Eu^{3+} ions the reason of which is Eu- Eu interactions and lattice defects are caused by non-radiative energy transfer among the superfluous Eu^{3+} activators.

Asymmetry factor defined as the intensity ratio of the $^5D_0 \rightarrow {}^7F_2$ to $^5D_0 \rightarrow {}^7F_1$ transition is widely used as a very sensitive and efficient probe to detect the local structure around Eu^{3+} [57]. Thus, in this work, the asymmetry factor of luminescence [$I(^5D_0 \rightarrow {}^7F_2)/I(^5D_0 \rightarrow {}^7F_1)$] was calculated from the PL spectra for the Eu^{3+} doped phosphors with different doping concentration and host lattice (Fig. S8). The asymmetry factors stay stable at ~6.6 and ~6.9 for hexagonal oxysulfide and monoclinic oxyslufate, respectively, indicating that the variation of doping concentration brings little influence on the distortion of Eu^{3+} ions. This may be due to the fact that there is only one site for Eu^{3+} to occupy in the two hosts, and the site symmetry is relatively low. The similarity of the asymmetry factor of Eu^{3+} in the two host lattices indicates the similar distortion degree of Eu^{3+} in the two host lattices. Comparatively speaking, for Eu^{3+} doped cubic oxide, with increasing concentration, the factor is increased from ~9.4 to ~10.8. The reason can be explained as followed: the increasing doping concentration favored the evenly distribution of Eu^{3+} cations, which allows the Eu^{3+} activators to move towards their crystallographic positions for Eu^{3+} substitution (C_2 and S_6). Since the $^5D_0 \rightarrow {}^7F_2$ emission arose from the C_2 site while the $^5D_0 \rightarrow {}^7F_1$ emission largely arose from the S_6 site for Eu^{3+}, the statistically much higher occupancy of the C_2 sites (the ratio of C_2 to S_6 is 3:1) results in an increased asymmetry factor, along with the increasing doping concentration. The higher factor of Gd_2O_3 than those of Gd_2O_2S and $Gd_2O_2SO_4$ indicates a deeper degree of distortion in its host lattice.

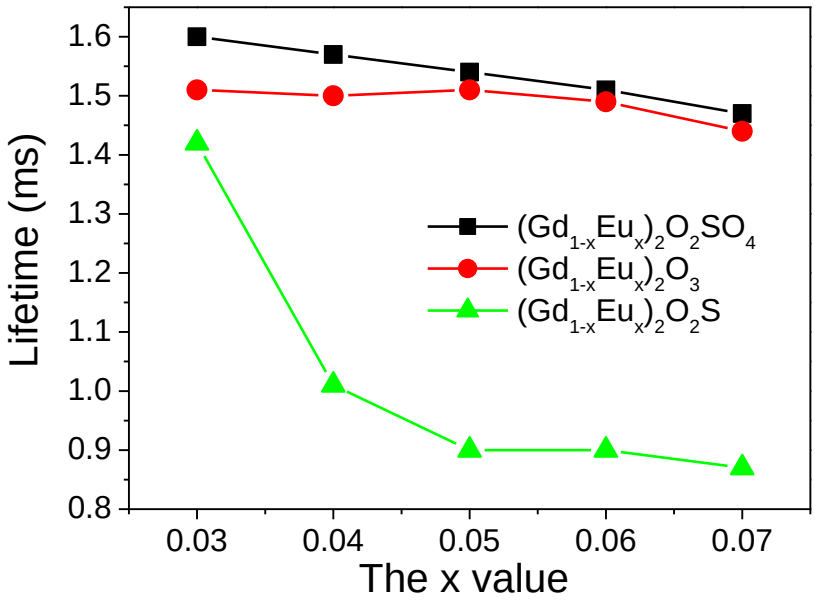

Fig. 11. Lifetime of the $^5D_0 \rightarrow {}^7F_2$ emission as a function of *x* value (Eu^{3+} content) in the $(Gd_{1-x}Eu_x)_2O_2SO_4$, $(Gd_{1-x}Eu_x)_2O_3$ and $(Gd_{1-x}Eu_x)_2O_2S$ red phosphors.

Fluorescence decay kinetics of the $^5D_0 \rightarrow {}^7F_2$ transitions for the phosphors were studied, and determined dependences are shown in Fig. S9. The resultant lifetimes of Eu^{3+} as a function of Eu^{3+} content in different host lattices are shown in Fig. 11. The exponential fittings yield successive shorter fluorescence lifetimes with increasing Eu^{3+} concentration for the three systems. The decreasing tendency is gentle in $(Gd_{1-x}Eu_x)_2O_2SO_4$ and $(Gd_{1-x}Eu_x)_2O_3$ and sharp in $(Gd_{1-x}Eu_x)_2O_2S$, and it corresponds well to the concentration quenching behaviors observed (Fig. 9). The lifetimes for $(Gd_{1-x}Eu_x)_2O_2SO_4$, $(Gd_{1-x}Eu_x)_2O_3$, and $(Gd_{1-x}Eu_x)_2O_2S$ obtained in this work generally agree with the previously reported values [50,51,58-60]. The decreased lifetime is mainly due to the formation of a resonance energy transfer network between Eu^{3+} with continued doping. The formed energy transfer network will advance the energy transfer from the inside to the radiation center of the surface and therefore a shorter lifetime is resulted. The comparatively shorter lifetime in $(Gd_{1-x}Eu_x)_2O_2S$ may be due to the shorter

Ln-Ln distance in this host lattice, which enhances the energy transfer between the rare earth ions, as analyzed before, and the higher calcination temperature. The lifetimes in $(Gd_{1-x}Eu_x)_2O_3$ are slightly smaller than those in $(Gd_{1-x}Eu_x)_2O_2SO_4$, and it is mainly due to the fact that the higher calcination temperature would favor the elimination of lattice defects and increase of crystal perfection.

Conclusions

The conditions of hydrothermal synthesis of the sulfate-typed LGdHs was investigated, and the LGdHs microplates were obtained at 120 °C with pH = 9.0. Three kinds of important red phosphors $(Gd_{1-x}Eu_x)_2O_2SO_4$, $(Gd_{1-x}Eu_x)_2O_3$, and $(Gd_{1-x}Eu_x)_2O_2S$ were obtained by controlled calcination of the LLnHs precursor. The influences of doping concentration and host lattice on the Eu^{3+} photoluminescence were studied in detail, and the main conclusions are as followed:

(1) Through adjusting the hydrothermal pH, the compounds $Gd_2(OH)_4SO_4{\cdot}nH_2O$ and $Gd_2(OH)_5(SO_4)_{0.5}{\cdot}nH_2O$ can be obtained. Under lower pH 7.0-9.0, the former compound is obtainable and the particle can be downsized by raising the pH of the reaction system. Higher pH of 10.0 favors the formation of $Gd_2(OH)_5(SO_4)_{0.5}{\cdot}nH_2O$. The calcination of LGdHs in the air from 400 to 1000 °C produced $Gd_2O_2SO_4$ *via* the removement of hydration water and dehydroxylation, and continued calcination to 1200 °C yielded cubic Gd_2O_3. The calcination of LGdHs from 800 °C to 1200 °C in hydrogen atmosphere leads to the formation of Gd_2O_2S.

⑵ The PLE spectra consisted of broad and stronger CT bands and sharper and weaker lines attributed to the *f*-*f* transitions. The CT behavior was significantly influenced by the host lattice, and broader CT band was observed in the $(Gd_{1-x}Eu_x)_2O_2S$ due to

additional stronger S-Eu CT excitation band, aside from the O-Eu one exists in the host. The *f-f* transitions are located at almost the same positions due to the well-shielded 4*f* shells. The strongest red emissions were found at 613, 618, and 626 nm for the $(Gd_{1-x}Eu_x)_2O_2SO_4$, $(Gd_{1-x}Eu_x)_2O_3$ and $(Gd_{1-x}Eu_x)_2O_2S$ red phosphors, respectively, which corresponds to the $^5D_0 \rightarrow {}^7F_2$ transition of Eu^{3+}.

(3) The optimal doping concentration of Eu^{3+} in Gd_2O_3 and $Gd_2O_2SO_4$ is 6% and 3% in Gd_2O_2S, and the quenching was governed by exchange interactions. The fluorescence kinetics analysis shows that the $^5D_0 \rightarrow {}^7F_2$ red emissions decay in a single exponential manner irrespective of host lattice and doping concentration, and successively shortened lifetimes were yielded with the increasing doping concentration.

Acknowledgements

This work is supported by the Natural Science Foundation of Liaoning Province (Grant No. 2020-MS-286).

References

[1] P.F. Du, L.X. Song, J. Xiong, Z.Q. Xi, D.L. Jin, L.C. Wang, Preparation and the luminescent properties of Tb^{3+}-Doped Gd_2O_3 fluorescent nanofibers via electrospinning, Nanotechnology 22(3) (2011) 035602.

[2] J. Xu, J. Luo, L. Zeng, Y. Tao, G. Li, C. Li, J. Liu, L. Zhou, S. Hu, J. Yang, F. Lin, J. Tang, Comparative study of red-emitting pyrophosphate phosphors: Site-selective replacement of Eu^{3+} and luminescent properties, Ceram. Int. 49(11) (2023) 17271-17282.

[3] Z.J. Li, X.P. Wang, H.J. Yu, C.C. Qiu, Y.Y. Zhang, J. Li, X.S. Lv, B. Liu, Q. Shi, Y.G. Yang, $SrLaGa_3O_7:Bi^{3+}/Eu^{3+}/Tb^{3+}$: A novel trichromatic phosphor for WLEDs, Ceram. Int. 49(2) (2023) 2894-2903.

[4] T. Ma, H. Chen, L. Yin, F. Lei, Y. Shi, J. Xie, L. Zhang, L. Fan, A novel Eu^{3+}-doped phosphor-in-glass for WLEDs and the effect of borophosphate matrix, J. Rare Earth. 41(2) (2023) 190-199.

[5] Z.G. Xia, Y.Y. Zhang, M.S. Molokeev, V.V. Atuchin, Structural and luminescence properties of yellow-emitting $NaScSi_2O_6$: Eu^{2+} phosphors: Eu^{2+} site preference analysis and generation of red emission by codoping Mn^{2+} for white-light-emitting diode applications, J. Phys. Chem. C 117(40) (2013) 20847-20854.

[6] V.V. Atuchin, A.S. Aleksandrovsky, O.D. Chimitova, A.S. Krylov, M.S. Molokeev, B.G. Bazarov, J.G. Bazarova, Z.G. Xia, Synthesis and spectroscopic properties of multiferroic β′-$Tb_2(MoO_4)_3$, Opt. Mater. 36(10) (2014) 1631-1635.

[7] Y.G. Denisenko, V.V. Atuchin, M.S. Molokeev, N.Z. Wang, X.X. Jiang, A.S. Aleksandrovsky, A.S. Krylov, A.S. Oreshonkov, A.E. Sedykh, S.S. Volkova, Z.S. Lin, O.V. Andreev, K. Müller-Buschbaum, Negative thermal expansion in one-dimension of a new double sulfate $AgHo(SO_4)_2$ with isolated SO_4 tetrahedra, J. Mater. Sci. Technol. 76 (2021) 111-121.

[8] V.A. Petrov, G.V. Kuptsov, A.O. Kuptsova, V.V. Atuchin, E.V. Stroganova, V.V. Petrov, Enhanced Yb: YAG Active Mirrors for High Power Laser Amplifiers, Photonics 10(7) (2023) 849.

[9] G. Xu, F. Liu, J. Lian, N. Wu, X. Zhang, J. He, Synthesis and optical properties of Eu^{3+} ion-doped $La_2O_2S_2$ via a solid state reaction method using $La_2O_2SO_4$ as a raw material, Ceram. Int. 44(15) (2018) 19070-19076.

[10] X.Z. Huang, Z. Liu, Y. Yang, Y. Tang, Molten salt synthesis of $La_2O_2SO_4$ nanosheets and their luminescent properties with Eu^{3+} doping, Funct. Mater. Lett. 6(2) (2013) 1350019.

[11] X. Luo, W. Cao, M. Xing, Preparation of nano Y_2O_2S: Eu phosphor by ethanol assisted combustion synthesis method, J. Rare Earth. 24(1) (2006) 20-24.

[12] X. Wang, M. Sun, Y. Fu, W. Liu, Q. Wang, C. Wang, J.G. Li, $Na(Gd,RE)(WO_4)_2$ double tungstates (RE= Eu/Yb-Er): crystallization from a novel layered hydroxide precursor and favorable luminescence for optical thermometry, J. Asian Ceram. Soc. 9(3) (2021) 782-793.

[13] S.A. Osseni, S. Lechevallier, M. Verelst, P. Perriat, J. Dexpert-Ghys, D. Neumeyer, R. Garcia, F. Mayer, K. Djanashvili, J.A. Peters, E. Magdeleine, H. Gros-Dagnac, P. Celsis, R. Mauricot, Gadolinium oxysulfide nanoparticles as multimodal imaging agents for T_2-weighted MR, X-ray tomography and photoluminescence, Nanoscale 6(1) (2014) 555-564.

[14] S.A. Osseni, S. Lechevallier, M. Verelst, C. Dujardin, J. Dexpert-Ghys, D. Neumeyer, M. Leclercq, H. Baaziz, D. Cussac, V. Santrane, R. Mauricot, New nanoplatform based on $Gd_2O_2S:Eu^{3+}$ core: synthesis, characterization and use for in vitro bio-labelling, J. Mater. Chem. 21(45) (2011) 18365-18372.

[15] M. Machida, K. Kawamura, K. Ito, K. Ikeue, Large-capacity oxygen storage by lanthanide oxysulfate/oxysulfide systems, Chem. Mater. 17(6) (2005) 1487-1492.

[16] M. Machida, T. Kawano, M. Eto, D. Zhang, K. Ikeue, Ln dependence of the large-capacity oxygen storage/release property of Ln oxysulfate/oxysulfide systems, Chem. Mater. 19(4) (2007) 954-960.

[17] D. Zhang, F. Yoshioka, K. Ikeue, M. Machida, Synthesis and oxygen

release/storage properties of Ce-substituted La-oxysulfates, $(La_{1-x}Ce_x)_2O_2SO_4$, Chem. Mater. 20(21) (2008) 6697-6703.

[18] J. Lian, F. Liu, X. Wang, X. Sun, Hydrothermal synthesis and photoluminescence properties of $Gd_2O_2SO_4$: Eu^{3+} spherical phosphor, Powder Technol. 253 (2014) 187-192.

[19] L. Song, P. Du, Q. Jiang, H. Cao, J. Xiong, Synthesis and luminescence of high-brightness $Gd_2O_2SO_4$: Tb^{3+} nanopieces and the enhanced luminescence by alkali metal ions co-doping, J. Lumin. 150 (2014) 50-54.

[20] F. Li, M. Jin, Z. Li, X. Wang, Q. Zhu, J.G. Li, Vertically aligned $Gd_2O_2SO_4$:Ln and Gd_2O_2S:Ln luminescent films with super-hydrophobicity via a novel precursor route (Ln = Pr, Eu, Tb), Appl. Surf. Sci. 609 (2023) 155323.

[21] J. Liang, R. Ma, F. Geng, Y. Ebina, T. Sasaki, $Ln_2(OH)_4SO_4 \cdot nH_2O$ (Ln = Pr to Tb; n~2): A new family of layered rare-earth hydroxides rigidly pillared by sulfate ions, Chem. Mater. 22(21) (2010) 6001-6007.

[22] F. Geng, R. Ma, Y. Matsushita, J. Liang, Y. Michiue, T. Sasaki, Structural study of a series of layered rare-earth hydroxide sulfates, Inorg. Chem. 50(14) (2011) 6667-6672.

[23] X. Wang, J.G. Li, Q. Zhu, X. Li, X. Sun, Y. Sakka, Facile and green synthesis of $(La_{0.95}Eu_{0.05})_2O_2S$ red phosphors with sulfate-ion pillared layered hydroxides as a new type of precursor: controlled hydrothermal processing, phase evolution and photoluminescence, Sci. Technol. Adv. Mater. 15(1) (2014) 014204.

[24] L. C. Thompson, Complexes, in Handbook on the Physics and Chemistry of Rare Earths, ed. K. A. Gschneidner, Jr. and L. Eyring, North-Holland Physics, Amsterdam, 1979.

[25] R.D. Shannon, Revised effective ionic radii and systematic studies of interatomic distances in halides and chalcogenides, Acta Crystallogr. A. 32(5) (1976) 751-767.

[26] L. Poudret, T.J. Prior, L.J. McIntyre, A.M. Fogg, Synthesis and crystal structures of new lanthanide hydroxyhalide anion exchange materials, $Ln_2(OH)_5X{\cdot}1.5H_2O$ (X = Cl, Br; Ln = Y, Dy, Er, Yb), Chem. Mater. 20(24) (2008) 7447-7453.

[27] Q. Zhu, J.G. Li, X. Li, X. Sun, Y. Qi, M. Zhu, Y. Sakka, Tens of micron-sized unilamellar nanosheets of Y/Eu layered rare-earth hydroxide: efficient exfoliation via fast anion exchange and their self-assembly into oriented oxide film with enhanced photoluminescence, Sci. Technol. Adv. Mat. 15(1) (2014) 014203.

[28] B. Lu, J.G. Li, T.S. Suzuki, M. Estili, W. Liu, X. Sun, Y. Sakka, Controlled synthesis of layered rare-earth hydroxide nanosheets leading to highly transparent $(Y_{0.95}Eu_{0.05})_2O_3$ ceramics, J. Am. Ceram. Soc. 98(5) (2015) 1413-1422.

[29] X. Wu, J.G. Li, Q. Zhu, W. Liu, J. Li, X. Li, X. Sun, Y. Sakka, One-step freezing temperature crystallization of layered rare-earth hydroxide ($Ln_2(OH)_5NO_3{\cdot}nH_2O$) nanosheets for a wide spectrum of Ln (Ln = Pr-Er, and Y), anion exchange with fluorine and sulfate, and microscopic coordination probed via photoluminescence, J. Mater. Chem. C. 3(14) (2015) 3428-3437.

[30] N.N. Golovnev, M.S. Molokeev, S.N. Vereshchagin, V.V. Atuchin, Calcium and strontium thiobarbiturates with discrete and polymeric structures, J. Coord. Chem. 66(23) (2013) 4119-4130.

[31] N.N. Golovnev, L.A. Solovyov, M.K. Lesnikov, S.N. Vereshchagin, V.V. Atuchin, Hydrated and anhydrous cobalt (II) barbiturates: Crystal structures, spectroscopic and thermal properties, Inorg. Chim. Acta 467 (2017) 39-45.

[32] Y.G. Denisenko, M.S. Molokeev, A.S. Oreshonkov, A.S. Krylov, A.S.

Aleksandrovsky, N.O. Azarapin, O.V. Andreev, I.A. Razumkova, V.V. Atuchin, Crystal structure, vibrational, spectroscopic and thermochemical properties of double sulfate crystalline hydrate $[CsEu(H_2O)_3(SO_4)_2]\cdot H_2O$ and its thermal dehydration product $CsEu(SO_4)_2$, Crystals 11(9) (2021) 1027.

[33] Y.G. Denisenko, M.S. Molokeev, A.S. Krylov, A.S. Aleksandrovsky, A.S. Oreshonkov, V.V. Atuchin, N.O. Azarapin, P.E. Plyusnin, E.I. Sal'nikova, O.V. Andreev, High-temperature oxidation of europium (II) sulfide, J. Indust. Eng. Chem. 79 (2019) 62-70.

[34] Y.G. Denisenko, A.E. Sedykh, S.A. Basova, V.V. Atuchin, M.S. Molokeev, A.S. Aleksandrovsky, A.S. Krylov, A.S. Oreshonkov, N.A. Khritokhin, E.I. Sal'nikova, O.V. Andreev, K. Müller-Buschbaum, Exploration of the structural, spectroscopic and thermal properties of double sulfate monohydrate $NaSm(SO_4)_2\cdot H_2O$ and its thermal decomposition product $NaSm(SO_4)_2$, Adv. Powder Technol. 32(11) (2021) 3943-3953.

[35] Y.G. Denisenko, V.V. Atuchin, M.S. Molokeev, A.E. Sedykh, N.A. Khritokhin, A.S. Aleksandrovsky, A.S. Oreshonkov, N.P. Shestakov, S.V. Adichtchev, A.M. Pugachev, E.I. Sal'nikova, O.V. Andreev, I.A. Razumkova, K. Müller-Buschbaum, Exploration of the crystal structure and thermal and spectroscopic properties of monoclinic praseodymium sulfate $Pr_2(SO_4)_3$, Molecules 27(13) (2022) 3966.

[36] W. Zachariasen, The crystal structure of the modification C of the sesquioxides of the rare earth metals, and of indium and thallium, Nor. Geol. Tidsskr. 9 (1927) 310-316.

[37] M. Onoda, X.-A. Chen, A. Sato, H. Wada, Crystal structure of $Cu_2Gd_{2/3}S_2$: interlayer short-range order of Gd vacancies, J. Solid State Chem. 152 (2000) 332-339.

[38] H.E. Hoefdraad, Charge-transfer spectra of tetravalent lanthanide ions in oxides, J. Inorg. Nucl. Chem. 37(9) (1975) 1917-1921.

[39] L. Li, S. Zhang, Dependence of charge transfer energy on crystal structure and composition in Eu^{3+}-doped compounds, J. Phys. Chem. B. 110(43) (2006) 21438-21443.

[40] V. Đorđević, Ž. Antićn, M.G. Nikolić, M.D. Dramićanin, Comparative structural and photoluminescent study of Eu^{3+}-doped La_2O_3 and $La(OH)_3$ nanocrystalline powders, J. Phys. Chem. Solids. 75(2) (2014) 276-282.

[41] P.L. Shi, Z.G. Xia, M.S. Molokeev, V.V. Atuchin, Crystal chemistry and luminescence properties of red-emitting $CsGd_{1-x}Eu_x(MoO_4)_2$ solid-solution phosphors, Dalton Trans. 43(25) (2014) 9669-9676.

[42] H.P. Ji, Z.H. Huang, Z.G. Xia, M.S. Molokeev, X.X. Jiang, Z.S. Line, V.V. Atuchin, Comparative investigations of the crystal structure and photoluminescence property of eulytite-type $Ba_3Eu(PO_4)_3$ and $Sr_3Eu(PO_4)_3$, Dalton Trans. 44(16) (2015) 7679-7686.

[43] J.G. Li, Y. Sakka, Recent progress in advanced optical materials based on gadolinium aluminate garnet ($Gd_3Al_5O_{12}$), Sci. Technol. Adv. Mater. 16(1) (2015) 014902.

[44] P. Dorenbos, The Eu^{3+} charge transfer energy and the relation with the band gap of compounds, J. Lumin. 111(1-2) (2005) 89-104.

[45] J.G. Li, X. Li, X. Sun, T. Ishigaki, Monodispersed colloidal spheres for uniform Y_2O_3:Eu^{3+} red-phosphor particles and greatly enhanced luminescence by simultaneous Gd^{3+} doping, J. Phys. Chem. C. 112(31) (2008) 11707-11716.

[46] V.V. Atuchin, A.S. Aleksandrovsky, O.D. Chimitova, T.A. Gavrilova, A.S. Krylov, M.S. Molokeev, A.S. Oreshonkov, B.G. Bazarov, J.G. Bazarova, Synthesis and spectroscopic properties of monoclinic α-$Eu_2(MoO_4)_3$, J. Phys. Chem. C 118(28) (2014) 15404-15411.

[47] Y.G. Denisenko, V.V. Atuchin, M.S. Molokeev, A.S. Aleksandrovsky, A.S. Krylov, A.S. Oreshonkov, S.S. Volkova, O.V. Andreev, Structure, thermal stability, and spectroscopic properties of triclinic double sulfate $AgEu(SO_4)_2$ with isolated SO_4 groups, Inorg. Chem. 57(21) (2018) 13279-13288.

[48] V.V. Atuchin, A.S. Aleksandrovsky, B.G. Bazarov, J.G. Bazarova, O.D. Chimitova, Y.G. Denisenko, T.A. Gavrilova, A.S. Krylov, E.A. Maximovskiy, M.S. Molokeev, A.S. Oreshonkov, A.M. Pugachev, N.V. Surovtsev, Exploration of structural, vibrational and spectroscopic properties of self-activated orthorhombic double molybdate $RbEu(MoO_4)_2$ with isolated MoO_4 units, J. Alloys Compd. 785 (2019) 692-697.

[49] Q. Zhu, J.G. Li, X. Li, X. Sun, Selective processing, structural characterization, and photoluminescence behaviors of single crystalline $(Gd_{1-x}Eu_x)_2O_3$ nanorods and nanotubes, Curr. Nanosci. 6(5) (2010) 496-504.

[50] Y. Song, H. You, Y. Huang, M. Yang, Y. Zheng, L. Zhang, N. Guo, Highly uniform and monodisperse $Gd_2O_2S:Ln^{3+}$ (Ln = Eu, Tb) submicrospheres: solvothermal synthesis and luminescence properties, Inorg. Chem. 49(24) (2010) 11499-11504.

[51] J. Lian, X. Sun, X. Li, Synthesis, characterization and photoluminescence properties of $(Gd_{1-x},Eu_x)_2O_2SO_4$ sub-microphosphors by homogeneous precipitation method, Mater. Chem. Phys. 125(3) (2011) 479-484.

[52] X. Lu, L. Yang, Q. Ma, J. Tian, X. Dong, A novel strategy to synthesize $Gd_2O_2S:Eu^{3+}$ luminescent nanobelts via inheriting the morphology of precursor, J. Mater. Sci. Mater. Electron. 25 (2014) 5388-5394.

[53] Q. Dai, H. Song, M. Wang, X. Bai, B. Dong, R. Qin, X. Qu, H. Zhang, Size and concentration effects on the photoluminescence of $La_2O_2S:Eu^{3+}$ Nanocrystals, J. Phys. Chem. C. 112(49) (2008) 19399-19404.

[54] J. Li, J.G. Li, S. Liu, X. Li, X. Sun, Y. Sakka, The development of Ce^{3+}-activated $(Gd,Lu)_3Al_5O_{12}$ garnet solid solutions as efficient yellow-emitting phosphors, Sci. Technol. Adv. Mater. 14(5) (2013) 054201.

[55] L.G. Van Uttert, L.F. Johnson, Energy transfer between rare-earth ions, J. Chem. Phys. 44(9) (1966) 3514-3522.

[56] L. Ozawa, Determination of self-concentration quenching mechanisms of rare earth luminescence from intensity measurements on powdered phosphor screens, J. Electrochem. Soc. 126(1) (1979) 106.

[57] G. Blasse, B.C. Grabmair, A general introduction to luminescent materials, Luminescent materials Berlin: Springer Verlag (1994).

[58] J. Lian, X. Sun, Z. Liu, J. Yu, X. Li, Synthesis and optical properties of $(Gd_{1-x},Eu_x)_2O_2SO_4$ nano-phosphors by a novel co-precipitation method, Mater. Res. Bull. 44(9) (2009) 1822-1827.

[59] O. Meza, E.G. Villabona-Leal, L.A. Diaz-Torres, H. Desirena, J.L. Rodríguez-López, E. Pérez, Luminescence concentration quenching mechanism in $Gd_2O_3:Eu^{3+}$, J. Phys. Chem. A 118(8) (2014) 1390-1396.

[60] R.M.K. Whiffen, Z. Antic´, A. Speghini, M.G. Brik, B. Bártová, M. Bettinelli, M.D. Dramićanin, Structural and spectroscopic studies of Eu^{3+} doped Lu_2O_3–Gd_2O_3 solid solutions, Opt. Mater. 36(6) (2014) 1083-1091.

Declaration of interests

☑The authors declare that they have no known competing financial interests or personal relationships that could have appeared to influence the work reported in this paper.

☐The authors declare the following financial interests/personal relationships which may be considered as potential competing interests: